

# Independent confirmation of a methane spike on Mars and a source region east of Gale Crater

Marco Giuranna<sup>1\*</sup>, Sébastien Viscardy<sup>2</sup>, Frank Daerden<sup>2</sup>, Lori Neary<sup>2</sup>, Giuseppe Etiope<sup>1,3,4</sup>, Dorothy Oehler<sup>5</sup>, Vittorio Formisano, Alessandro Aronica<sup>1</sup>, Paulina Wolkenberg<sup>1,6</sup>, Shohei Aoki<sup>1,2,7,8</sup>, Alejandro Cardesín-Moinelo<sup>9</sup>, Julia Marín-Yaseli de la Parra<sup>9</sup>, Donald Merritt<sup>9</sup> and Marilena Amoroso<sup>10</sup>

**Reports of methane detection in the Martian atmosphere have been intensely debated. The presence of methane could enhance habitability and may even be a signature of life. However, no detection has been confirmed with independent measurements. Here, we report a firm detection of  $15.5 \pm 2.5$  ppb by volume of methane in the Martian atmosphere above Gale Crater on 16 June 2013, by the Planetary Fourier Spectrometer onboard Mars Express, one day after the in situ observation of a methane spike by the Curiosity rover. Methane was not detected in other orbital passages. The detection uses improved observational geometry, as well as more sophisticated data treatment and analysis, and constitutes a contemporaneous, independent detection of methane. We perform ensemble simulations of the Martian atmosphere, using stochastic gas release scenarios to identify a potential source region east of Gale Crater. Our independent geological analysis also points to a source in this region, where faults of Aeolis Mensae may extend into proposed shallow ice of the Medusae Fossae Formation and episodically release gas trapped below or within the ice. Our identification of a probable release location will provide focus for future investigations into the origin of methane on Mars.**

Since its discovery in the Martian atmosphere<sup>1–4</sup>, there has been a continuing debate about the origin of methane (CH<sub>4</sub>), and several generation mechanisms—both abiotic and biotic—have been proposed<sup>5–17</sup>. Despite various detections reported by separate groups and different experiments, the methane debate still splits the Mars community. Although plausible mechanisms have been proposed to explain the observed abundance, variability and lifetime of methane in the current Martian atmosphere<sup>18–34</sup>, doubts about its very existence still arise. Previous detections have been considered tentative<sup>35</sup> due to either the challenge of discriminating telluric and Martian features when observing from Earth (claims later rebutted<sup>23</sup>) or the limited spectral resolving power and/or signal-to-noise ratio of space-borne observations<sup>18–20</sup>. In situ detection of CH<sub>4</sub> at Gale Crater<sup>1</sup> by the Tunable Laser Spectrometer-Sample Analysis at Mars (TLS-SAM) on Curiosity has also been questioned<sup>36</sup> as potentially coming from the rover itself, although that possibility was ruled out by the Curiosity team<sup>24</sup>. However, while several non-detections have been reported, none of the positive detections have been confirmed so far with independent measurements.

## Methane detection by the Planetary Fourier Spectrometer (PFS)

The Mars Express (MEx) spacecraft<sup>37</sup> was designed to operate in several science pointing modes, including nadir pointing and spot pointing. Most PFS<sup>38</sup> observations are acquired in nadir pointing<sup>2,18,19</sup>. The spot-tracking mode, which points the optical instruments to a surface feature on Mars and tracks it, was exploited in this study for the first time. These observations are particularly suitable for methane retrievals because they allow acquisition of sev-

eral hundred spectra over one area in a relatively short time (typically, a few tens of minutes). The ensemble average of these measurements enhances the statistical importance of the PFS observations, as detailed in the Supplementary Information 1. In Supplementary Table 1, we summarize the list of spot-tracking observations over Gale Crater performed by the PFS from December 2012 to July 2014, which roughly corresponds to the first 20-month period of methane measurements at Gale Crater by Curiosity's TLS-SAM<sup>4</sup>.

PFS observed elevated levels of methane of  $15.5 \pm 2.5$  ppb by volume (ppbv) column-integrated abundance, in orbit 12025, on 16 June 2013 (Table 1). This date just follows Martian solar day (sol) 305 after the landing of the Curiosity rover<sup>24</sup>, when the TLS-SAM also reported a methane spike of  $5.78 \pm 2.27$  ppbv. Therefore, our results are evidence of the contemporaneous detection of methane in the Martian atmosphere by in situ and remote sensing measurements. In Fig. 1a, we show the PFS average spectrum for orbit 12025 (280 measurements collected in about 45 min in spot-tracking mode) compared with synthetic best-fit spectra. In Fig. 1b, we subtract the synthetic best-fit spectrum with no methane from the PFS spectrum. The CH<sub>4</sub> absorption band observed by PFS becomes evident in the differential spectrum (Fig. 1b). The relatively high spectral resolution and the new data handling allow unambiguous identification of the CH<sub>4</sub> Q-branch at  $3,018 \text{ cm}^{-1}$  by the PFS near-infrared spectra. Considering the  $1\sigma$  uncertainty, methane abundances ranging from 13–18 ppbv are consistent with the observed intensity of the CH<sub>4</sub> absorption band. A detailed description of the new PFS data treatment and improved characterization of the PFS apodized instrument line shape is reported in Supplementary Information 1. The algorithm adopted for the CH<sub>4</sub> retrievals is described in the Methods.

<sup>1</sup>Istituto di Astrofisica e Planetologia Spaziali, Istituto Nazionale di Astrofisica, Rome, Italy. <sup>2</sup>Royal Belgian Institute for Space Aeronomy, Brussels, Belgium.

<sup>3</sup>Istituto Nazionale di Geofisica e Vulcanologia, Rome, Italy. <sup>4</sup>Faculty of Environmental Science and Engineering, Babes-Bolyai University, Cluj-Napoca, Romania. <sup>5</sup>Planetary Science Institute, Tucson, AZ, USA. <sup>6</sup>Centrum Badań Kosmicznych Polska Akademia Nauk, Warsaw, Poland. <sup>7</sup>Fonds National de la Recherche Scientifique, Brussels, Belgium. <sup>8</sup>Department of Geophysics, Tohoku University, Sendai, Japan. <sup>9</sup>European Space Astronomy Centre, Madrid, Spain. <sup>10</sup>Agenzia Spaziale Italiana, Sede di Matera, Italy. \*e-mail: [marco.giuranna@iaps.inaf.it](mailto:marco.giuranna@iaps.inaf.it)

**Table 1 | List of observational constraints**

Sols <sup>a</sup>	Date <sup>b</sup>	Time	MEx orbit <sup>c</sup>	Value (ppbv)	Instrument
-1	Sol 304	-9:45 <sup>d</sup> (LTST)	12018	≤3 ppbv	PFS
0	Sol 305	13:00 <sup>e</sup> (LTST); ingestion: 20'	NA	5.78 ± 2.27	TLS-SAM
1	Sol 306	9:41 <sup>e</sup> (LTST); measurement duration: 43'	12025 <sup>f</sup>	15.5 ± 2.5	PFS
8	Sol 313	NA	NA	2.13 ± 2.02	TLS-SAM
11	Sol 316	-9:24 <sup>d</sup> (LTST)	12060	≤5	PFS
13	Sol 318	-9:19 <sup>d</sup> (LTST)	12067	≤5	PFS

<sup>a</sup>Number of sols before (negative values) or after the TLS-SAM measurements on sol 305. Upper limits are provided (1 $\sigma$  uncertainty) when no CH<sub>4</sub> band was observed in the PFS spectra. <sup>b</sup>Sols since the Mars Science Laboratory landing (sol 305=15 June 2013). <sup>c</sup>Orbit tracks and PFS footprints are shown in Supplementary Fig. 12a. <sup>d</sup>Average time of orbit. <sup>e</sup>Starting time of observation. <sup>f</sup>Spot-tracking observation. LTST, local true solar time. NA, not available.

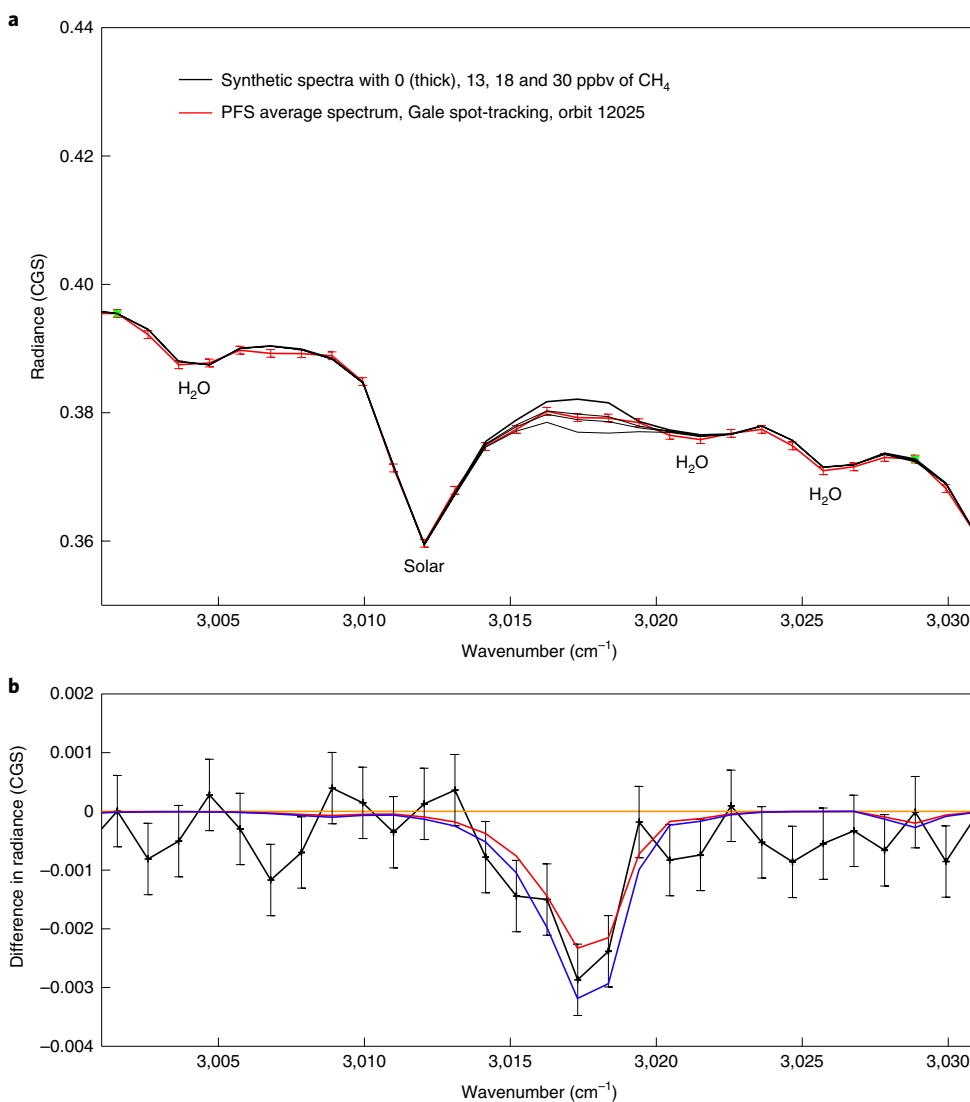


**Fig. 1 | PFS retrieval of CH<sub>4</sub> abundance from orbit 12025.** **a**, Synthetic best-fit spectra (black curves) are compared with the PFS average spectrum (red). H<sub>2</sub>O abundance is 350 ppm in all spectra. Water vapour and solar lines are also indicated. The two green spots indicate the spectral points used to retrieve the surface albedo (see Methods). **b**, The best-fit synthetic spectrum with 0 ppbv of methane shown in **a** is subtracted from the PFS average spectrum (black) and from the synthetic spectra with 13 and 18 ppbv of methane (red and blue curves, respectively). The orange line marks the zero level. 1 $\sigma$  error bars are shown in **a** and **b** (see Supplementary Information 1 for details). CGS, centimetre-gram-second system of units.

In the almost 2-year period of spot-tracking observations reported here (22 in total), there was no other occasion on which PFS made a positive detection of methane over Gale Crater (see

Supplementary Table 1). PFS did not perform any spot-tracking observations during the second TLS-SAM high-methane period (sol 466 to sol 526), but there were 10 spot-tracking observations

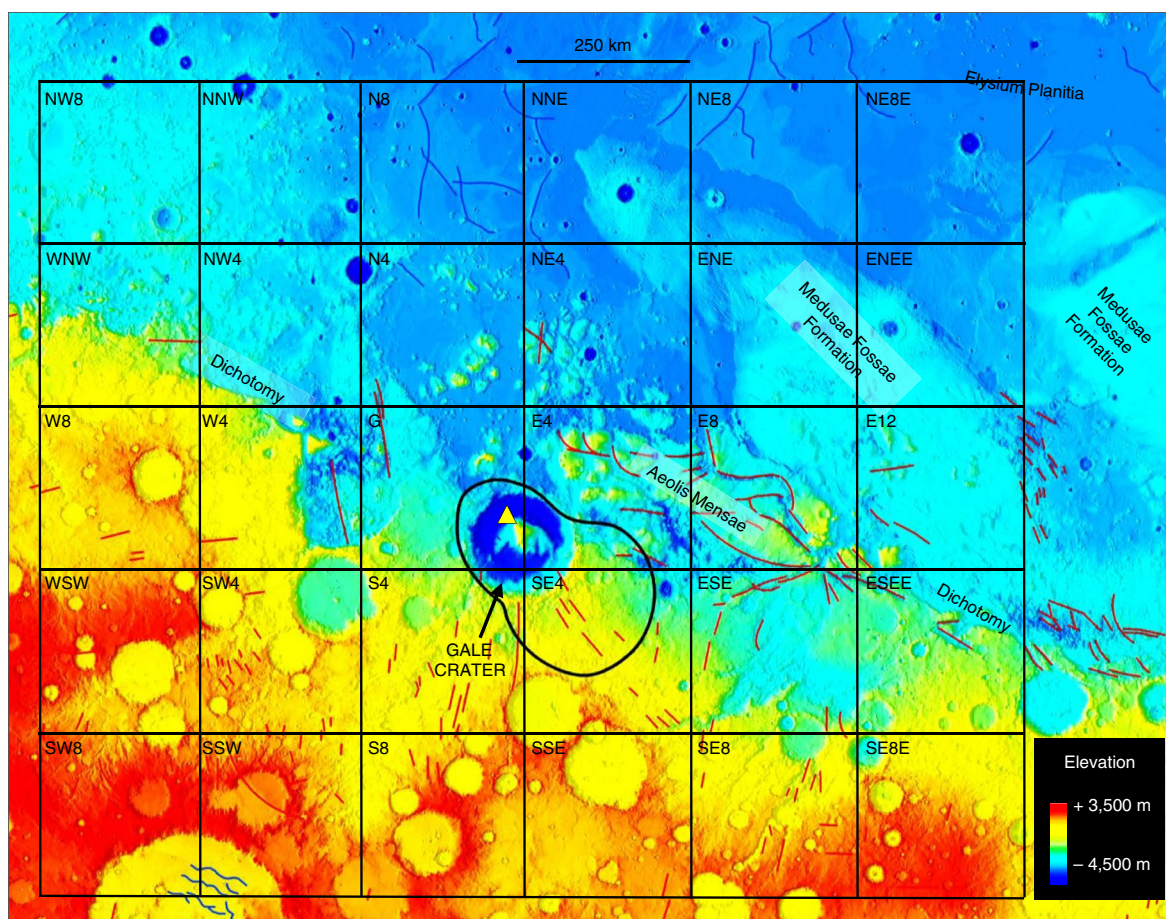


**Fig. 2 | Location map and regional setting.** Basemap of MOLA elevation on MOLA Hillshade. The black grid shows the area of interest from atmospheric modelling. Red lines show extensional faults, while blue lines show compressional faults<sup>48</sup>. The black outline around Gale Crater is the envelope of PFS footprints for orbit 12025. The yellow triangle shows the location of the Curiosity rover. The label of each emission site is indicated in the top left corner of the 30 blocks. The emission sites are labelled according to their location with respect to Block G, which stands for Gale Crater as it covers the largest part of the crater, and the grid spacing in degrees (such that ESE = East South East; E8 = 8° East).

in the later period when no methane was detected, with a detection limit of 2–4 ppbv. This is consistent with the low methane measurements by TLS-SAM in the same period. In addition, no evidence of methane was found in three nadir observations performed a few days apart from sol 306 in the area surrounding Gale Crater (Table 1 and Supplementary Fig. 12a). An example of non-detection is shown in Supplementary Fig. 12b for MEx orbit 12018 (one sol before the TLS-SAM spike detection on sol 305; Table 1). An upper limit of 3 ppbv of CH<sub>4</sub> is retrieved from the average of 276 PFS measurements collected in this orbit.

### The search for CH<sub>4</sub> source regions

The contemporaneous detection of methane provides unique information to use in the search for its source locations. The available data in a 14-sol time window (sols 304–318; Table 1) provide evidence that the sol 305–306 observations by the PFS and TLS-SAM sampled the same methane release event, and that this event is limited in time. Although several production mechanisms and sources of methane have been discussed in the literature<sup>6–17</sup>, terrestrial analogues argue that subsurface accumulations are the most likely sources (see Supplementary Information 2). Subsurface methane could have been produced by either abiotic or biotic processes and stored in clathrates, zeolites or reservoir rocks (any permeable or fractured rock) sealed by permafrost or other impermeable rocks before being outgassed through fractures and faults<sup>16</sup>. Accordingly, in this paper, we focus on the hypothesis of surface

release. Exogenous processes that may add methane to the Martian atmosphere<sup>17</sup> are not considered in this work.

It has been argued that a gas emission possibly explaining the detection by TLS-SAM on sol 305 was probably weak and local (possibly inside the crater) and took place to the north of Curiosity because the prevailing daytime near-surface winds are southwards<sup>4</sup>. However, the vertically integrated methane abundance measured by PFS one sol later changes our understanding of the release event. The amount of methane measured by PFS corresponds to ~39–54 tonnes that were present in the area of ~49,000 km<sup>2</sup> observed from orbit (Fig. 2). The combination of PFS and TLS observations strongly suggests that the emission took place outside the crater (see Supplementary Information 3), making a general circulation model (GCM) an appropriate choice for a first interpretation of these observations. To simulate methane transport, we applied the three-dimensional Global Environmental Multiscale (GEM)-Mars model<sup>28,39,40</sup> (see Methods). Wind fields simulated in the GCM show variability with local time and height (see Supplementary Fig. 17), increasing the complexity of methane transport compared with previous assumptions<sup>4</sup>.

The search for the source of methane based on a few observations is an under-constrained problem. The constraints provided by the available observations (Table 1) suggest that the release event was relatively short and occurred not very far from the crater. As methane is rapidly dispersed after its release<sup>28</sup>, a distant source would require very large amounts of methane to be emitted to be

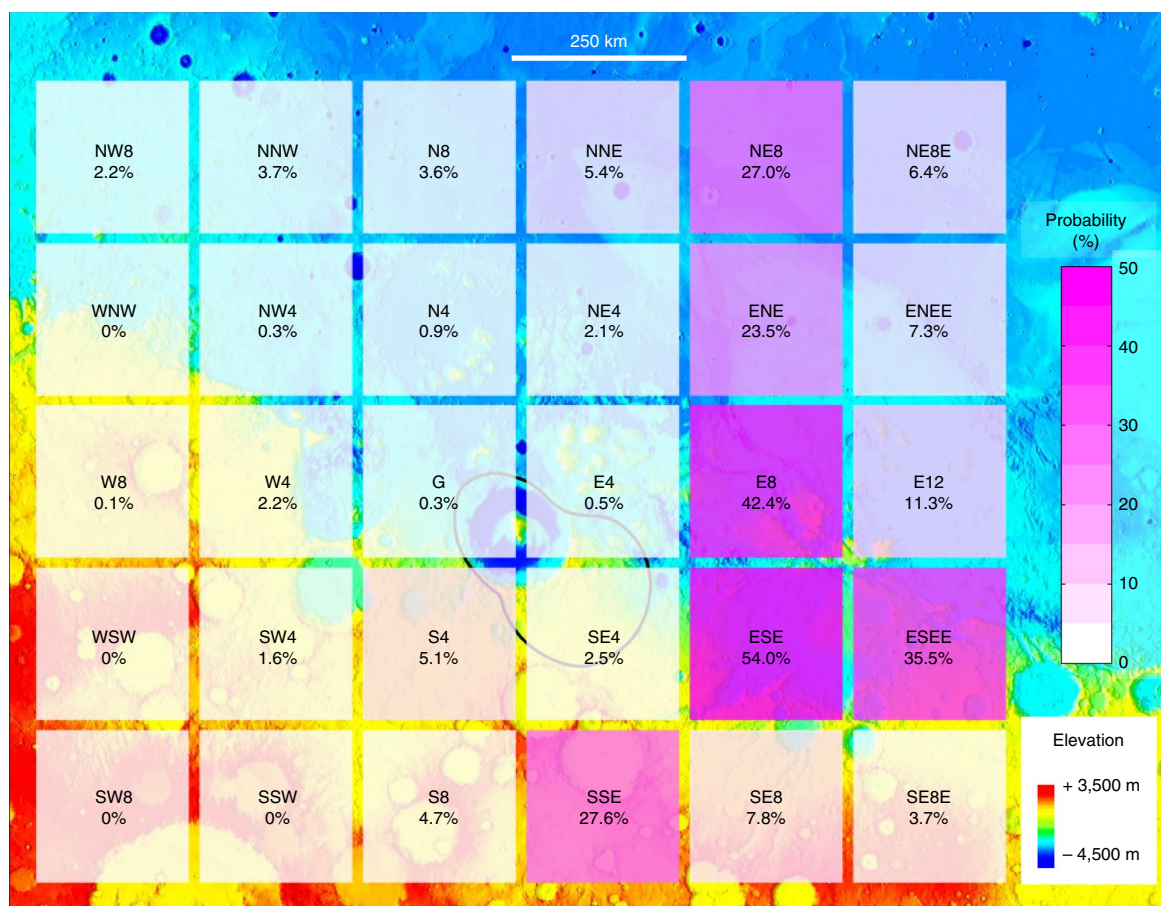


**Fig. 3 | Probabilities estimated for the 30 emission sites.** For each grid cell, the probability of being a source location is defined as the number of release scenarios consistent with the observations divided by the sample size. Basemap as in Fig. 2.

able to reach the crater, which would be inconsistent with the observational constraints. Preliminary model tests led to the following assumptions that restrict the problem: (1) the source is unlikely to be more distant than ~800 km from the crater; and (2) the emission did not start before sol 302. We considered 30 model grid cells within a  $24^\circ \times 20^\circ$  area centred at Gale Crater as potential emission sites (Fig. 2). The problem remains weakly constrained as no direct information is available on the source's location, or the initial time, duration, temporal variations and strengths of gas fluxes characterizing the release pattern. For this reason, we developed an ensemble approach, considering a very large sample of possible emission scenarios, to identify the most likely sources in terms of probability.

We considered methane emission patterns (release intensity, duration and temporal variation) that are based on gas seepage theory and consistent with methane seepage phenomena observed on Earth<sup>41</sup> (see Supplementary Information 2 for details). We assumed an 'episodic' seepage scenario for the methane release (Supplementary Fig. 7), which is most consistent with previous detections<sup>1–4</sup>. An episodic emission may be characterized by one single major pulse or a series of short-term seepage oscillations (Supplementary Information 2). From each of the 30 possible emission sites considered in the model, a series of 30-min-long methane pulses was applied for a total duration of 5 sols (from sol 302 to 307). Exploiting the linear additivity of the methane tracers (as the methane is chemically inert on the considered timescale, and the feedback of methane on the atmospheric dynamics is negligible), the tracers were linearly combined by random numbers to produce release scenarios composed of stochastic fluxes. A total of  $10^6$  different combinations were generated for each of the 30 considered

release sites. For these patterns, the initial times and durations of emission were also generated randomly. As a result, the constructed episodic emission scenarios last from 30 min to 5 sols. The large number ( $10^6$ ) of emission scenarios considered in each of the model grid cells forms a statistically representative sample of all of the possible release scenarios from a specific site (Supplementary Fig. 16).

The simulated scenarios were then compared with the observational constraints in Table 1. The number of scenarios consistent with the observations divided by the sample size then gives the probability that a methane release from a given emission site fits the observations (see Methods). The result is shown in a probability map (Fig. 3). Sites to the north, west and south-west of Gale Crater have no significant probability of being source locations. Sites to the east and south-east of Gale Crater yield the highest probabilities as source locations, especially blocks E8 and ESE, with probabilities of 42.4% and 54.0%, respectively, meaning that about half of all the generated emission patterns released from these sites can reproduce the entire set of observations in Table 1. The total mass of methane released from E8 (ESE) in 95% of scenarios fitting the observations is 1,170–2,740 tonnes (1,590–4,050 tonnes), which corresponds to an enhancement of ~0.1–0.3 ppbv (0.2–0.4 ppbv) to the global mean mixing ratio, after the gas is well mixed around the planet. These abundances can be considered as upper limits for the mass released, given the coarse resolution of the GCM.

### Geological context

We investigated the Martian geological context in search of structures that might be associated with methane release (for example, faults, hydrothermal-volcanic vents, springs and mud volcanoes<sup>16</sup>),

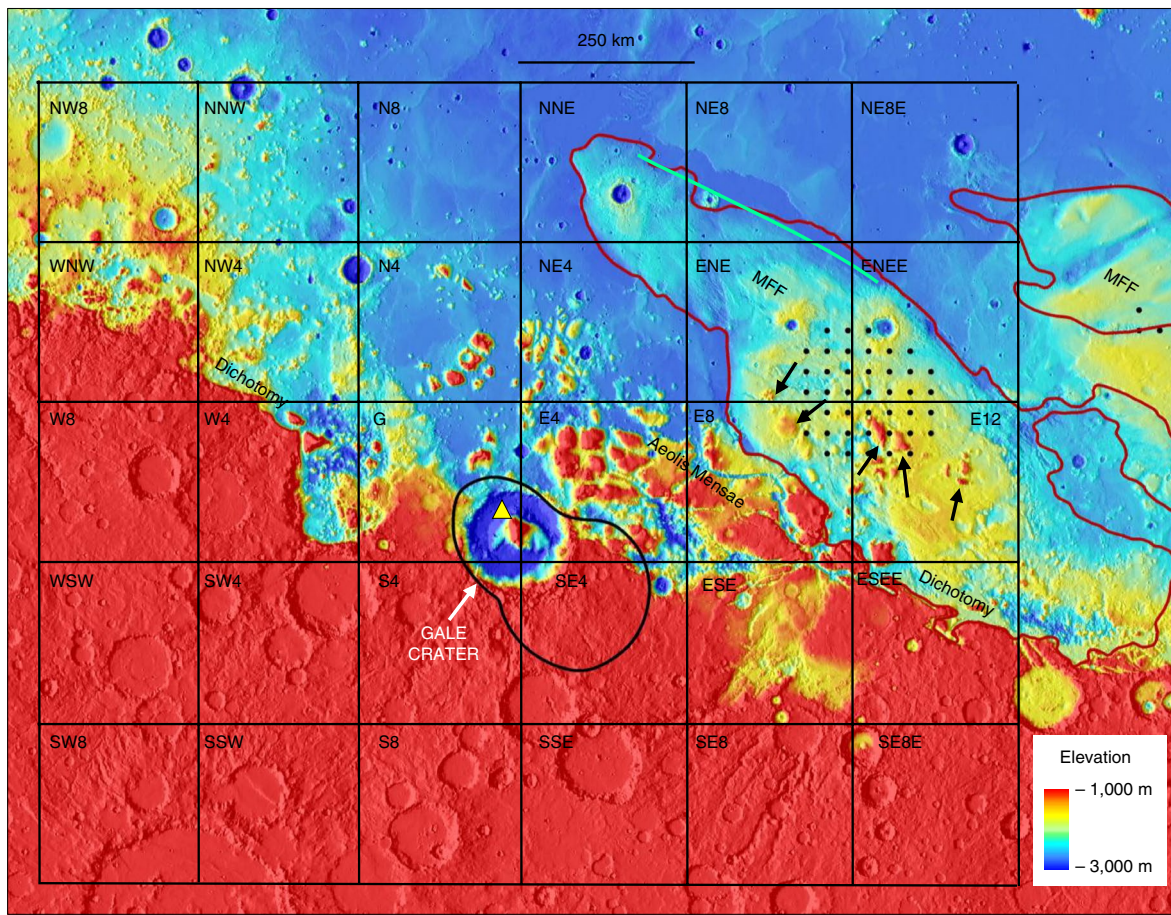


**Fig. 4 | Geological context of grid blocks.** Basemap of stretched MOLA elevation over MOLA Hillshade. Black dots represent sites with water-equivalent hydrogen > 26%<sup>43</sup>. The dark red line shows the outline of the lower member of the MFF. The green line shows aligned knobs<sup>49,50</sup>. Black arrows highlight Aeolis Mensae outcrops within the MFF. The yellow triangle is the Curiosity rover location.

applying knowledge of the relationships between gas seepage and tectonic/morphological structures, as observed on Earth<sup>41</sup>. Gas seepage occurs along faults of any type, regardless of the tectonic conditions. Details of terrestrial gas seepage and geological assessment of the Martian area of interest determined from atmospheric modelling (Fig. 2) are provided in Supplementary Information 2. Conclusions about the relative merits of different grid blocks were reached independent of the GCM analysis, by a separate team.

Potential methane release structures were identified along the eastern side of the grid, in block E8 and subordinately in blocks ENE, E12, ESE and ESEE (Fig. 4). Block E8 includes the Noachian–Hesperian fretted terrain of Aeolis Mensae<sup>42</sup>, in contact with the younger Hesperian–Amazonian Medusae Fossae Formation (MFF) and in close proximity to locations where the MFF has been proposed to contain shallow bulk ice (from water-equivalent hydrogen > ~26%<sup>43</sup>). Since permafrost is one of the best seals for methane<sup>16</sup>, it is possible that bulk ice in the MFF may trap and seal subsurface methane. That methane could be released episodically along faults that break through the permafrost due to partial melting of ice, gas pressure build-up induced by gas accumulation during migration, or stresses due to planetary adjustments or local meteorite impact<sup>16</sup> (see also Supplementary Information 2). The distribution of geological outcrops suggests that Aeolis Mensae deposits underlie the area of bulk ice (Fig. 4). Faults of Aeolis Mensae, being associated with the Martian dichotomy, may be deeply rooted<sup>16</sup> (Supplementary Information 2) and may have provided long-lived conduits for migrating methane and liquid water, the latter perhaps contributing to accumulation of shallow ice in the MFF. In addition, the many

fault intersections of Aeolis Mensae may enhance permeability and thus degassing, as on Earth<sup>41</sup>. Several lineations appear to offset dunes and yardangs in the MFF of block E8 (Supplementary Fig. 8) and may be relatively recent. These lineations have orientations similar to faults of Aeolis Mensae and may be surface expressions of reactivated Aeolis Mensae/dichotomy faults at depth, providing pathways for gas seepage through an otherwise sealing permafrost.

Blocks ESE and ESEE contain extensions of Aeolis Mensae dichotomy faults in their north-eastern and northern portions, respectively. Block ESE is farther from the bulk ice (Fig. 4) than block E8, and block ESEE is still farther. Block ESE, however, contains unusual flow-like structures (Supplementary Fig. 8), and we are continuing to assess whether these might be methane release structures. Other blocks are of lesser merit (see Supplementary Information 2).

Thus, the eastern sector of the grid contains features that could trap subsurface methane and account for its present-day, episodic release. Of these, block E8 is the highest ranked, as it has potentially recent faults closest to the proposed ice. Because the area affected by faults and ice is large ( $10^2$ – $10^4$  km<sup>2</sup>; Fig. 4), methane flux from either diffuse microseepage or seeps along faults in the ice could account for the methane detected by the PFS (see Supplementary Information 2 and Supplementary Fig. 10).

### A first step to understanding the origin of methane on Mars

This work presents the first independent confirmation of methane detection on Mars and the first synergistic approach to the

search for potential sites of methane release, integrating orbital and ground-based detections with Martian geology and atmospheric simulations (using gas emission scenarios based on terrestrial seepage data). This approach provides a template for future efforts aimed at locating sites of methane release from the subsurface on Mars. While this work relies on the hypothesis of a surface release, other explanations remain possible, but given a surface release, our work provides the first constraints for source locations.

The results of the GCM and geological analyses are remarkable, as each line of investigation independently pointed to the same area east/southeast of Gale as the most likely source location for the methane (Figs. 3 and 4). Block E8 is singled out, as it contains multiple faults and fault intersections of Aeolis Mensae, along with possible extensions of those faults into proposed shallow ice in the overlying MFF. Such ice could have sealed subsurface methane, and recent reactivation of Aeolis Mensae/dichotomy faults could have penetrated the ice, episodically opening enhanced release pathways.

The results presented in this work not only corroborate previous detections by Curiosity but, in a broader perspective, might change our view of methane occurrence on Mars. Rather than by large emissions and a global presence, our data suggest that the presence of methane on Mars might be characterized by small, short emissions and transient events. This possibility has been raised before<sup>35,41</sup>, but further investigations are required to understand processes of rapid methane loss and reconcile these new PFS findings with the anticipated Trace Gas Orbiter results<sup>44</sup>.

We do not address the ultimate origin of the detected Martian methane. Many abiotic and biotic processes can generate methane on Mars<sup>6–17</sup>. However, the first step to understanding the origin of any Martian methane is to determine its release location. From there, detailed follow-up should eventually reveal the mode of generation and significance of detected methane<sup>45</sup>. The PFS instrument will continue its monitoring of the Martian atmosphere. The new approach, described here, to PFS data selection, processing and retrieval will also be applied to the entire PFS dataset for a complete reanalysis. In addition, spot-tracking observations will be performed over geologically determined potential source regions of methane, including the region identified in this work, providing a test of the model of subsurface release. The ExoMars Trace Gas Orbiter payload<sup>46,47</sup> will also continue its search for methane from Mars' orbit, and coordinated observations with PFS are being planned.

### Online content

Any methods, additional references, Nature Research reporting summaries, source data, statements of data availability and associated accession codes are available at <https://doi.org/10.1038/s41561-019-0331-9>.

Received: 14 July 2018; Accepted: 18 February 2019;  
Published online: 1 April 2019

### References

- Krasnopolsky, V. A., Maillard, J. P. & Owen, T. C. Detection of methane in the Martian atmosphere: evidence for life? *Icarus* **172**, 537–547 (2004).
- Formisano, V., Atreya, S., Encrenaz, T., Ignatiev, N. & Giuranna, M. Detection of methane in the atmosphere of Mars. *Science* **306**, 1758–1761 (2004).
- Mumma, M. J. et al. Strong release of methane on Mars in northern summer 2003. *Science* **323**, 1041–1045 (2009).
- Webster, C. R. et al. Mars methane detection and variability at Gale Crater. *Science* **347**, 415–417 (2015).
- Yung, Y. et al. Methane on Mars and habitability: challenges and responses. *Astrobiology* **18**, 1221–1242 (2018).
- Atreya, S. K., Mahaffy, P. R. & Wong, A. S. Methane and related trace species on Mars: origin, loss, implications for life, and habitability. *Planet. Space Sci.* **55**, 358–369 (2007).
- Oze, C. & Sharma, M. Have olivine, will gas: serpentinization and the abiogenic production of methane on Mars. *Geophys. Res. Lett.* **32**, L10203 (2005).
- Krasnopolsky, V. A. Some problems related to the origin of methane on Mars. *Icarus* **180**, 359–367 (2006).
- Chassefière, E. Metastable methane clathrate particles as a source of methane to the Martian atmosphere. *Icarus* **204**, 137–144 (2009).
- Gough, R. V., Tolbert, M. A., McKay, C. P. & Toon, O. B. Methane adsorption on a Martian soil analog: an abiogenic explanation for methane variability in the Martian atmosphere. *Icarus* **207**, 165–174 (2010).
- Meslin, P.-Y., Gough, R., Lèfevre, L. & Forget, F. Little variability of methane on Mars induced by adsorption in the regolith. *Planet. Space Sci.* **59**, 247–258 (2011).
- Keppeler, F. et al. Ultraviolet-radiation-induced methane emissions from meteorites and the Martian atmosphere. *Nature* **486**, 93–96 (2012).
- Schuerger, A., Moores, J. E., Clausen, C. A., Barlow, N. G. & Britt, D. T. Methane from UV-irradiated carbonaceous chondrites under simulated Martian conditions. *J. Geophys. Res.* **117**, E08007 (2012).
- McMahon, S., Parnell, J. & Blamey, N. J. F. Sampling methane in basalt on Earth and Mars. *Int. J. Astrobiol.* **12**, 113–122 (2013).
- Poch, O., Kaci, S., Stalport, F., Szopa, C. & Coll, P. Laboratory insights into the chemical and kinetic evolution of several organic molecules under simulated Mars surface UV radiation conditions. *Icarus* **242**, 50–63 (2014).
- Oehler, D. Z. & Etiope, G. Methane seepage on Mars: where to look and why. *Astrobiology* **17**, 1233–1264 (2017).
- Fries, M. et al. A cometary origin for Martian atmospheric methane. *Geochem. Perspect. Lett.* **2**, 10–23 (2016).
- Geminale, A., Formisano, V. & Giuranna, M. Methane in Martian atmosphere: average spatial, diurnal, and seasonal behavior. *Planet. Space Sci.* **56**, 1194–2003 (2008).
- Geminale, A., Formisano, V. & Sindoni, G. Mapping methane in Martian atmosphere with PFS-MEx data. *Planet. Space Sci.* **59**, 137–148 (2011).
- Fonti, S. & Marzo, G. A. Mapping the methane on Mars. *Astron. Astrophys.* **512**, A51 (2010).
- Krasnopolsky, V. A. A sensitive search for methane and ethane on Mars. In *EPSC-DPS Joint Meeting 2011* (Copernicus, 2011).
- Krasnopolsky, V. A. Search for methane and upper limits to ethane and SO<sub>2</sub> on Mars. *Icarus* **217**, 144–152 (2012).
- Villanueva, G. L. et al. A sensitive search for organics (CH<sub>4</sub>, CH<sub>3</sub>OH, H<sub>2</sub>CO, C<sub>2</sub>H<sub>6</sub>, C<sub>2</sub>H<sub>2</sub>, C<sub>2</sub>H<sub>4</sub>), hydroperoxyl (HO<sub>2</sub>), nitrogen compounds (N<sub>2</sub>O, NH<sub>3</sub>, HCN) and chlorine species (HCl, CH<sub>2</sub>Cl) on Mars using ground-based high-resolution infrared spectroscopy. *Icarus* **223**, 11–27 (2013).
- Webster, C. R. et al. Background levels of methane in Mars' atmosphere show strong seasonal variations. *Science* **360**, 1093–1096 (2018).
- Summers, M. E., Lieb, B. J., Chapman, E. & Yung, Y. L. Atmospheric biomarkers of subsurface life on Mars. *Geophys. Res. Lett.* **29**, 2171 (2002).
- Lefèvre, F. & Forget, F. Observed variations of methane on Mars unexplained by known atmospheric chemistry and physics. *Nature* **460**, 720–723 (2009).
- Atreya, S. K. et al. Methane on Mars: current observations, interpretations, and future plans. *Planet. Space Sci.* **59**, 133–136 (2011).
- Viscardy, S., Daerden, F. & Neary, L. Formation of layers of methane in the atmosphere of Mars after surface release. *Geophys. Res. Lett.* **43**, 1868–1875 (2016).
- Holmes, J. A., Patel, M. R. & Lewis, S. R. The vertical transport of methane from different potential emission types on Mars. *Geophys. Res. Lett.* **44**, 8611–8620 (2017).
- Holmes, J. A., Lewis, S. R. & Patel, M. R. Analyzing the consistency of Martian methane observations by investigation of global methane transport. *Icarus* **257**, 23–32 (2015).
- Farrell, W. M., Delory, G. T. & Atreya, S. K. Martian dust storms as a possible sink of atmospheric methane. *J. Geophys. Res.* **33**, L21203 (2006).
- Atreya, S. K. et al. Oxidant enhancement in Martian dust devils and storms: implications for life and habitability. *Astrobiology* **6**, 439–450 (2006).
- Delory, G. T. et al. Oxidant enhancement in Martian dust devils and storms: storm electric fields and electron dissociative attachment. *Astrobiology* **6**, 451–462 (2006).
- Knak Jensen, S. J. et al. A sink for methane on Mars? The answer is blowing in the wind. *Icarus* **236**, 24–27 (2014).
- Zahnle, K. J., Freedman, R. S. & Catling, D. C. Is there methane on Mars? *Icarus* **212**, 493–503 (2011).
- Zahnle, K. J. Play it again, SAM. *Science* **347**, 370–371 (2015).
- Wilson, A. & Chicarro, A. *Mars Express: The Scientific Payload SP-1240* (European Space Agency, 2004).
- Formisano, V. et al. The Planetary Fourier Spectrometer (PFS) onboard the European Mars Express mission. *Planet. Space Sci.* **53**, 963–974 (2005).
- Neary, L. & Daerden, F. The GEM-Mars general circulation model for Mars: description and evaluation. *Icarus* **300**, 458–476 (2018).
- Daerden, F. et al. A solar escalator on Mars: self-lifting of dust layers by radiative heating. *Geophys. Res. Lett.* **42**, 7319–7326 (2015).
- Etiope, G. & Oehler, D. Z. Methane spikes, background seasonality and non-detections on Mars: a geological perspective. *Planet. Space Sci.* <https://doi.org/10.1016/j.pss.2019.02.001> (in the press).

42. Kerber, L. & Head, J. W. The age of the Medusae Fossae Formation: evidence of Hesperian emplacement from crater morphology, stratigraphy, and ancient lava contacts. *Icarus* **206**, 669–684 (2010).
43. Wilson, J. T. et al. Equatorial locations of water on Mars: improved resolution maps based on Mars Odyssey Neutron Spectrometer data. *Icarus* **299**, 148–160 (2018).
44. Voosen, P. Martian methane—spotted in 2004—has mysteriously vanished. *Science* <http://doi.org/10.1126/science.aaw3667> (2018).
45. Etioppe, G. Understanding the origin of methane on Mars through isotopic and molecular data from the ExoMars orbiter. *Planet. Space Sci.* **159**, 93–96 (2018).
46. Vandaele, A. C. et al. NOMAD, an integrated suite of three spectrometers for the ExoMars Trace Gas Mission: technical description, science objectives and expected performance. *Space Sci. Rev.* **214**, 80 (2018).
47. Korabiev, O. et al. The Atmospheric Chemistry Suite (ACS) of three spectrometers for the ExoMars 2016 Trace Gas Orbiter. *Space Sci. Rev.* **214**, 7 (2018).
48. Knapmeyer, M. et al. Working models for spatial distribution and level of Mars' seismicity. *J. Geophys. Res.* **111**, E11006 (2006).
49. Lanz, J. K. & Saric, M. B. Cone fields in SW Elysium Planitia: hydrothermal venting on Mars. *J. Geophys. Res.* **114**, E02008 (2009).
50. Martínez-Alonso, S., Mellon, M. T., McEwen, A. S. & the HiRISE Team. Geological study of a section of Aeolis Mensae, a possible site favorable for life. In *7th International Conference on Mars Abstract* 1353, 3262 (2007).

### Acknowledgements

We thank Environment and Climate Change Canada for providing the GEM model for research purposes, and for support. We thank J. T. Wilson for providing the data used to map the water-equivalent hydrogen from improved-resolution Mars Odyssey Neutron Spectrometer data. We thank O. Witasse, D. Titov, P. Martin and the ESA Science Ground Segment and Flight Control teams for successful operation of the MEX mission over more than a decade. The PFS experiment was built at the Institute for Space Astrophysics and Planetology (formerly the Institute for Interplanetary Space Physics) of the National Institute for Astrophysics, and is currently funded by the Italian Space Agency (agreement number 2018-2-HH.0) in the context of the science activities for the Nadir and Occultation for Mars Discovery spectrometer and the Atmospheric

Chemistry Suite onboard the Trace Gas Orbiter ExoMars 2016, and for PFS-MEX. D.O. is supported by the Planetary Science Institute. S.V. and L.N. are supported by the ESA PRODEX Office (contract number Prodex\_NOMADMarsScience\_C4000121493\_2017-2019). S.V. is also supported by the 'Excellence of Science' project 'Evolution and Tracers of Habitability on Mars and the Earth' (FNRS 30442502). P.W. is supported by the 'UPWARDS' project, funded from the European Union's Horizon 2020 research and innovation programme under grant agreement number 633127. S.A. has been supported by the FNRS 'CRAMIC' project under grant agreement number T.0171.16. This paper is dedicated to our colleague, V. Formisano, who recently passed away.

### Author contributions

M.G. and S.A. developed the new approach to PFS data selection and treatment. M.G. performed the CH<sub>4</sub> retrieval. A.A., P.W. and S.A. supervised the PFS science operations, planning, commanding and data archiving. A.C.-M. provided ancillary data and other geometrically relevant models for PFS and MEX through the SPICE software suite. A.C.-M., J.M.-Y.L.P. and D.M. contributed to planning the PFS observations and successful implementation and execution of the PFS spot-tracking observations. V.F. developed the concept and was the former principal investigator for PFS-MEX. S.V., F.D. and L.N. developed and performed the GCM simulations and analysis. G.E. and D.O. performed the geological analysis and evaluation of terrestrial seepage patterns. M.A. was responsible for the PFS-MEX project from the Italian Space Agency side. All authors contributed to interpretation of the results and preparation of the manuscript.

### Competing interests

The authors declare no competing interests.

### Additional information

**Supplementary information** is available for this paper at <https://doi.org/10.1038/s41561-019-0331-9>.

**Reprints and permissions information** is available at [www.nature.com/reprints](http://www.nature.com/reprints).

**Correspondence and requests for materials** should be addressed to M.G.

**Publisher's note:** Springer Nature remains neutral with regard to jurisdictional claims in published maps and institutional affiliations.

© The Author(s), under exclusive licence to Springer Nature Limited 2019

## Methods

**Computation of synthetic spectra and CH<sub>4</sub> retrieval algorithm.** We developed an algorithm to retrieve methane abundance (volume mixing ratio) on Mars from the PFS short wavelength channel (SWC) spectra. The algorithm includes a radiative transfer code developed for the analysis of PFS SWC spectra with a full treatment of the multiple scattering problem. The retrieval algorithm relies on the Levenberg–Marquardt approach<sup>51,52</sup>.

The computation of synthetic spectra relies on the DISORT (Discrete Ordinates Radiative Transfer Program for a Multi-Layered Plane-Parallel Medium) solver implemented in the ARS code<sup>53</sup> and specifically developed for the analysis of PFS spectra. DISORT is a general and versatile plane-parallel radiative transfer program applicable to problems from the ultraviolet to the radar regions of the electromagnetic spectrum<sup>54</sup>, which includes a full treatment of atmospheric multiple scattering by suspended particles. The synthetic spectra are obtained by performing the line-by-line computation, then filtering the result with the newly retrieved PFS apodized instrumental line shape described above. We use HITRAN 2012 (ref. <sup>55</sup>) as the spectroscopic database. The absorption coefficients  $k(\nu, p, T)$  at the  $i$ th atmospheric layer ( $\text{cm}^{-1}$ ) are defined as:

$$k_i(\nu, p, T) = \text{ACS}_i(\nu, p, T_i) \times n_i$$

where  $\nu$  is the wavenumber ( $\text{cm}^{-1}$ ), and  $P_i$  and  $T_i$  are the pressure (mbar) and temperature (K) at the  $i$ th layer, respectively. ACS<sub>*i*</sub> is the absorption cross section calculated from HITRAN 2012 using a Voigt profile ( $\text{cm}^{-1}/(\text{molecule} \times \text{cm}^{-2})/\text{cm}^{-1}$ ), and  $n_i$  is the number density ( $\text{cm}^{-3}$ ) calculated from the pressure and temperature using the perfect gas law. The absorption coefficients are calculated using a line-by-line approach<sup>54</sup>.

The use of an appropriate solar spectrum is also important for analysis of infrared spectra—in particular with relatively high spectral resolution—because Fraunhofer lines mix up with H<sub>2</sub>O absorption features in the considered spectral range. The PFS team has made a significant effort to construct a high-resolution Solar spectrum<sup>56</sup> used in this analysis. The commonly used spectrum<sup>57</sup> has disadvantages, being purely theoretical within the H<sub>2</sub>O bands, and under-sampled for our purpose (1  $\text{cm}^{-1}$  bins).

To calculate the synthetic spectra, a series of parameters that describe the atmospheric layers at the time of the observations must be specified as input parameters to the radiative transfer code. The initial guess for the H<sub>2</sub>O abundance (vertical profile) and surface pressure are the only parameters extracted from the GCM (EMCD version 5.2; refs. <sup>58,59</sup>) at the time (solar longitude ( $L_s$ ) and local time) and location (latitude and longitude) of the PFS measurements. For the surface pressure, we make use of pres0, a routine tool that estimates surface pressure with high accuracy using high-resolution (32 pix  $\text{deg}^{-1}$ ) Mars Orbiter Laser Altimeter (MOLA) topography, provided with EMCD 5.2. The initial abundance of methane is set to 0 ppbv. All of the other relevant atmospheric parameters (namely, the atmospheric temperature profile as a function of pressure and altitude), along with surface temperature and integrated dust and water ice opacity, are retrieved<sup>60,61</sup> from the PFS LWC measurements acquired simultaneously with those of the SWC used for the CH<sub>4</sub> retrievals.

To retrieve methane abundance, the synthetic spectra calculated as described above are best-fitted to the PFS average spectra. The retrieval algorithm relies on the minimization of the sum of the squares of the differences between the measured radiances and a parameterized function (least-squares problem). To solve the nonlinear least-squares problem, we adopt the Levenberg–Marquardt approach<sup>51,52</sup>.

To retrieve the methane mixing ratio, we use PFS SWC average spectra in the reduced spectral range 3,001–3,031  $\text{cm}^{-1}$ , which includes several absorption bands of water vapour, a solar band, and the CH<sub>4</sub> Q-branch at 3,018  $\text{cm}^{-1}$  (for example, see Supplementary Figs. 2, 5 and 6). Three parameters are considered in the iterative retrieval: the surface albedo, water abundance and methane mixing ratio. The goodness of fit between radiance measurements and synthetic spectra is checked at each iteration using the chi-squared error criterion  $\chi^2(a)$ . The improvements  $\Delta a$  of a retrieved parameter  $a$  are performed using the non-dimensional scalar factor  $\lambda$  presented in the formula:

$$[J^T W J + \lambda \times \text{diag}(J^T W J)] \times \Delta a = J^T W (y - y') \quad (1)$$

where  $J$  is the Jacobian matrix (a derivative of the fitted function with respect to each parameter), exponent T stands for transposed matrix,  $W$  is the inverse of the measurement error covariance matrix,  $y$  is the measured spectrum and  $y'$  is the synthetic spectrum.

The steps required and implemented in our algorithm for the Levenberg–Marquardt approach<sup>62</sup> can be summarized as follows:

- (1) Calculate the  $\chi^2(a)$  using a first guess of the parameters  $a$  to be retrieved;
- (2) Calculate  $\Delta a$  using equation (1), assuming an initial modest value for  $\lambda$  in the first iteration:  $\lambda = \lambda_0$ ;
- (3) Calculate the synthetic spectrum with updated parameters  $a + \Delta a$ ;
- (4) Evaluate  $\chi^2(a + \Delta a)$ ;
- (5) Update the value of  $\lambda$ . If  $\chi^2(a + \Delta a) \geq \chi^2(a)$ , increase  $\lambda$  by a ‘substantial’ factor  $f_+$ :  $\lambda_{i+1} = \lambda_i \times f_+$ , ( $i$  is the iteration number). If  $\chi^2(a + \Delta a) < \chi^2(a)$ , decrease  $\lambda$  by a ‘substantial’ factor  $f_-$ :  $\lambda_{i+1} = \lambda_i / f_-$ ;
- (6) Repeat steps (3)–(5) until a final solution is approached;
- (7) The algorithm is stopped when the convergence criterion is reached.

The Levenberg–Marquardt parameters  $\lambda_0$ ,  $f_+$ , and  $f_-$  have been estimated from preliminary tests on the retrieval algorithm by assuming a wide range of possible values and by the comparison of  $\chi^2(a)$  and  $\chi^2(a + \Delta a)$  in the various iterations. A good compromise between accuracy of retrieval (minimization of  $\chi^2(a)$ ), number of iterations required to reach the convergence criterion, and the required computational time is found for the following values of the above parameters, which have been adopted in the final implementation of the algorithm:  $\lambda_0 = 10^{-2}$ ;  $f_+ = 10^2$  and  $f_- = 10$ .

Also necessary is a condition for stopping. Iterating to convergence (to machine accuracy or to the round-off limit) is generally wasteful and unnecessary since the minimum is, at best, only a statistical estimate of the parameters ( $a$ ). A change in the parameters that changes  $\chi^2$  by an amount much less than 1 is never statistically meaningful<sup>61</sup>. In practice, it is recommended to stop iterating on the first or second occasion that decreases by a negligible amount, being either less than 0.01 absolutely or, in case round-off prevents that being reached, some fractional amount such as  $10^{-3}$  (ref. <sup>62</sup>). It is also recommended to avoid a stop after a step where  $\chi^2$  increases: this only shows that it has not yet adjusted itself optimally<sup>61</sup>. In our case, as a convergence criterion, we stop iterating when the following conditions are satisfied:  $\chi^2(a + \Delta a) - \chi^2(a) < 0$  and  $|\chi^2(a + \Delta a) - \chi^2(a)| < \chi^2(a + \Delta a) \times 10^{-3}$ .

We applied the retrieval algorithm described above to the PFS spot-tracking observations over Gale Crater listed in Supplementary Table 1, as well as to the standard nadir observations listed in Table 1. Only dayside observations with  $>200$  measurements were considered. Methane is only detected in orbit 12025, where PFS collected 280 measurements in about 45 min in spot-tracking mode. The results are shown in Fig. 1. The actual footprints of PFS observations and retrieved atmospheric temperature profiles used as input for the computation of synthetic spectra are shown in Supplementary Fig. 9a,b.

**GCM simulations.** The GEM-Mars three-dimensional GCM for the atmosphere of Mars<sup>39</sup> applied in this work was operated at a  $4^\circ \times 4^\circ$  horizontal resolution and with 103 vertical levels extending from the surface to  $\sim 7 \times 10^{-6}$  Pa ( $\sim 140$  km). The vertical resolution in the lowermost atmosphere is fine: the spacing between levels is  $\sim 15$  m near the surface and  $\sim 1$  km at 10 km in height. The model time step is 1/48 of a sol ( $\sim 30$  min). The model was extensively validated against multiple datasets<sup>39</sup>, and was previously applied for the study of fine dust layers observed by the Phoenix Mars mission<sup>40</sup>, the simulation of the annual cycles of water vapour and carbon monoxide on Mars<sup>63</sup>, the simulation of the Mars dust cycle<sup>64</sup>, and the transport of methane on surface release<sup>38</sup>. GEM-Mars forms an integral part in the analysis and interpretation of data from the Nadir and Occultation for Mars Discovery spectrometer on the European Space Agency (ESA)–Roskosmos ExoMars Trace Gas Orbiter<sup>44,65–67</sup>.

The accuracy of the simulated wind fields can be optimized by constraining the dynamical model fields by available observations. To do this, the atmospheric dust content in the GCM was imposed to be in accordance with the dust observations by the PFS obtained during MEx orbits 12018 (nadir) and 12025 (spot-tracking) (Table 1 and Supplementary Fig. 9c). GEM-Mars has an active dust lifting scheme, but the simulated dust optical depth was scaled at all times to the climatological values for Martian year 31 (ref. <sup>68</sup>), binned over  $L_s = 10^\circ$ . In the region of Gale Crater, the climatological value for  $L_s = 330$ – $340^\circ$  (optical depth = 0.62) was considerably larger than that measured by PFS (average optical depth:  $\sim 0.30$ ). The model dust optical depth was scaled globally in this time window by the ratio 0.30/0.62 to ensure that the dust optical depth in the Gale Crater area matches the PFS value at the time of the observations (Supplementary Fig. 9c). It was verified that the simulated temperature profile at the time of the PFS observation matched with the PFS retrieved temperature profile during orbit 12025 (Supplementary Fig. 9b). The model temperature profile shown in Supplementary Fig. 9b is an average of 70 profiles that are randomly distributed within the PFS orbit 12025 footprint (Supplementary Fig. 9a) at 09:40 local true solar time on sol 306. These model profiles were interpolated from the model grid and corrected for pressure, taking into account the height difference between the coarse-grained model grid and the high-resolution MOLA topography.

For each of the 30 grid cells considered as emission sites, a simulation was performed involving the release of 120 tracers (see below). The simulations were fully parallelized on 24 nodes of the Royal Belgian Institute for Space Aeronomy’s High-Performance Cluster.

**Statistical approach.** The statistical approach adopted here, belonging to the Monte Carlo-type approaches, is based on the assumption that the inert tracers (such as methane, on the considered timescales) simulated in a GCM are linearly additive. This was explicitly verified by test simulations (relative error of  $\sim 0.05\%$ ). As a corollary, they can also be scaled by any factor. In addition, while the model time step is  $\sim 30$  min, the average of two tracers released at an interval of one hour describes fairly well the evolution of the tracer released in between (relative error of  $\sim 3\%$ ). In practice, in this model study, 120 tracers were released successively every hour from any model grid cell. Exploiting the last assumption, the tracers released at the 119 model time steps in between can be reasonably considered as the average of tracers on both sides, so raising to 239 the total number of available tracers.

Let  $N = 239$  and  $M_i = 10^3$  kg be, respectively, the number of tracers and initial mass of each tracer  $T_i$  released at time  $t_i$ . If the mass of tracer  $T_i$  is scaled by a factor  $\varphi_i(t_i)$  arbitrarily chosen, the mass  $M_{0i}$  of  $T_i$  released into the atmosphere becomes:  $M_{0i} = \varphi_i(t_i) M_i$ .

To match the first and last observational constraints (Table 1), it was verified from test simulations that the event started at the earliest at midnight on sol 302 and lasted no longer than until the end of sol 306. In contrast, the event started necessarily before sol 305 at 13 h (that is, at the time of the methane detection by Curiosity). Finally, the minimum emission duration is 30 Mars minutes (that is, one model time step). Thus, with  $t_0$  being the initial time and  $\tau$  the duration of the event, we have:

$$0 \text{ h} \leq t_0 \leq 85 \text{ h} \text{ (that is, between sol 302 at 0 h and sol 305 at 13 h)}$$

$$\tau_{\min} \leq \tau \leq \tau_{\max}, \quad \text{where} \quad \begin{cases} \tau_{\min} = 30 \text{ min} \\ \tau_{\max} = 5 \text{ sols} \end{cases}$$

where  $\tau_{\min}$  and  $\tau_{\max}$  are the minimum and maximum durations, respectively. As a result, depending on  $t_0$  and  $\tau$ ,  $T_i(t_i)$  is zeroed if its emission time  $t_i$  is outside the time period of the event. These conditions can be rewritten in terms of Heaviside step functions as:

$$\theta_1(t_i - t_0) = \begin{cases} 1, & t_i \geq t_0 \\ 0, & t_i < t_0 \end{cases}$$

$$\theta_2(t_0 + \tau - t_i) = \begin{cases} 1, & t_i \leq t_0 + \tau \\ 0, & t_i > t_0 + \tau \end{cases}$$

and the effective mass  $M_{0i}$  of  $T_i$  released at time  $t_i$  takes the form:

$$M_{0i} = \varphi_i(t_p, t_0, \tau) M_r = \varphi_i(t_i) \theta_1(t_i - t_0) \theta_2(t_0 + \tau - t_i) M_r \\ = \begin{cases} \varphi_i(t_i) M_r, & t_0 \leq t_i \leq t_0 + \tau \\ 0, & t_i < t_0 \text{ or } t_i > t_0 + \tau \end{cases}$$

The total mass  $M_0$  of tracers released during the event occurring between  $t_0$  and  $t_0 + \tau$  is thus given by:

$$M_0 = \sum_{i=1}^N \varphi_i(t_p, t_0, \tau) M_r$$

For the sake of conciseness, Greek and Latin letters will indicate the measurements (retrieved abundance of methane) and the corresponding model variables (mean abundance for the same area and temporal interval of the observations), respectively. Let  $\{\alpha, \beta, \gamma, \delta, \epsilon, \zeta\}$  be the set of observational constraints reported in Table 1:

$$\begin{aligned} \text{MSL(sol 305)} : \alpha \pm \Delta\alpha &= 5.78 \pm 2.27 \text{ ppbv} \\ \text{PFS(sol 306)} : \beta \pm \Delta\beta &= 15.5 \pm 2.5 \text{ ppbv} \\ \text{MSL(sol 313)} : \gamma \pm \Delta\gamma &= 2.13 \pm 2.02 \text{ ppbv} \\ \text{PFS(sol 304)} : \delta &= 3 \text{ ppbv} \\ \text{PFS(sol 316)} : \epsilon &= 5 \text{ ppbv} \\ \text{PFS(sol 318)} : \zeta &= 5 \text{ ppbv} \end{aligned}$$

Let  $\{A, B, C, D, E, F\}$  be the set of model variables that must fit the observational dataset  $\{\alpha, \beta, \gamma, \delta, \epsilon, \zeta\}$ . A release scenario is said to be consistent with the observations if and only if the following relations are satisfied:

$$\begin{cases} \alpha - \Delta\alpha \leq A \leq \alpha + \Delta\alpha \\ \beta - \Delta\beta \leq B \leq \beta + \Delta\beta \\ \gamma - \Delta\gamma \leq C \leq \gamma + \Delta\gamma \\ 0 \leq D \leq \delta \\ 0 \leq E \leq \epsilon \\ 0 \leq F \leq \zeta \end{cases}$$

Let  $\{A_{0i}, B_{0i}, C_{0i}, D_{0i}, E_{0i}, F_{0i}\}$  be the set of model variables that result from the emission of the initial mass  $M_r$  of the single tracer  $T_r$ . Those variables are obtained by linear interpolation at the time and location of the corresponding observations. As they depend linearly on  $M_{0i}$ , they are scaled by the same factor  $\varphi_i(t_p, t_0, \tau)$ . Consequently, the model variables  $\{A_0, B_0, C_0, D_0, E_0, F_0\}$  can be written as:

$$\begin{cases} A_0 = \sum_{i=1}^N \varphi_i(t_p, t_0, \tau) A_{0i} \\ B_0 = \sum_{i=1}^N \varphi_i(t_p, t_0, \tau) B_{0i} \\ \vdots \\ F_0 = \sum_{i=1}^N \varphi_i(t_p, t_0, \tau) F_{0i} \end{cases}$$

We generate  $10^6$  potential release events for each of the 30 emission sites considered by generating the same number of random combinations of the parameters  $\varphi_i, t_0, \tau$ . Then, for each single event, the model variables can be scaled by a factor  $f$  to match the observations, when possible. This factor must satisfy six constraining relations in terms of the six observations:

$$\begin{cases} \frac{\alpha - \Delta\alpha}{A_0} \leq f \leq \frac{\alpha + \Delta\alpha}{A_0} \\ \frac{\beta - \Delta\beta}{B_0} \leq f \leq \frac{\beta + \Delta\beta}{B_0} \\ \frac{\gamma - \Delta\gamma}{C_0} \leq f \leq \frac{\gamma + \Delta\gamma}{C_0} \\ 0 \leq f_D \leq \frac{\delta}{D} \\ 0 \leq f_E \leq \frac{\epsilon}{E} \\ 0 \leq f_F \leq \frac{\zeta}{F} \end{cases}$$

or, more simply:

$$f_{\min} \leq f \leq f_{\max}$$

where  $f = \{f_A, f_B, f_C, f_D, f_E, f_F\}$ .

A scenario is said to be consistent with the observations if it exists  $f$  such that:

$$\max(f_{\min}) \leq f \leq \min(f_{\max})$$

If so,  $f$  is arbitrarily chosen as the mean value between  $\max(f_{\min})$  and  $\min(f_{\max})$ :

$$f = \frac{\max(f_{\min}) + \min(f_{\max})}{2}$$

As described above, a sequence of stochastic fluxes is generated to produce a release pattern that mimics an episodic seepage event. In practice, this procedure consists in generating random factors  $\{\varphi_i(t_i)\}$  given by a probability distribution function.  $\varphi_i(t_i)$  is defined as the factor scaling the initial mass  $M_r$  of tracer  $T_r$ , so that:

$$\varphi_i(t_i) = \frac{M_{0i}}{M_r}$$

If a mass  $M_{0i}$  is released from a surface area  $S$  during one model time step  $\Delta t$ , the resulting release rate  $\chi_{0i}(t_i)$  of  $T_i$  is given by:

$$\chi_{0i}(t_i) = \frac{M_{0i}}{S\Delta t}$$

Therefore,  $\varphi_i(t_i)$  takes the form:

$$\varphi_i(t_i) = \frac{S\Delta t}{M_r} \chi_{0i}(t_i)$$

Let  $P(\chi)$  be a probability distribution function of the release rate  $\chi$  used to randomly generate a release pattern. Given that the time evolution of gas fluxes is not known, even on Earth, we chose the simplest function (that is, the uniform distribution function):

$$P_u(\chi) = \frac{1}{X_0}; 0 \leq \chi \leq X_0$$

where  $X_0$  is fixed to  $150 \text{ mg m}^{-2} \text{ d}^{-1}$ . This value is arbitrary but does not affect the final results because the tracers are all scaled by a factor  $f$  afterwards. Any other distribution function could be used. In our study, to test the sensitivity of the analysis to the variability of gas fluxes, and to estimate the robustness of the statistical results, we also considered a Gaussian distribution function:

$$P_G(\chi) = \frac{1}{\sqrt{2\pi\sigma^2}} \exp\left[-\frac{(\chi - \mu)^2}{2\sigma^2}\right]; 0 \leq \chi \leq \infty$$

where  $\mu = 75 \text{ mg m}^{-2} \text{ d}^{-1}$  and  $\sigma = 20 \text{ mg m}^{-2} \text{ d}^{-1}$ . The good agreement between the so-obtained probability map (not shown) and that displayed in Fig. 3 indicates that the probabilities of fitting the observations do not depend dramatically on the gas flux variability, which emphasizes the robustness of our results.

Finally, the initial time  $t_0$  and duration  $\tau$  of the release event are generated randomly using a uniform distribution function.

An example scenario is presented in Supplementary Figs. 13–15. Supplementary Fig. 13 illustrates the procedure followed to produce one release pattern. Supplementary Fig. 14 shows the time evolution of the simulated methane abundance at Gale Crater and the procedure to scale the tracers to match the observations. Supplementary Fig. 15 finally shows maps of the simulated methane abundance for the times of the available observations.

**Geological analysis.** For the GCM simulations, we considered terrestrially realistic methane emission patterns (that is, release intensity, duration, variation and area) based on gas seepage theory and experimental data acquired on Earth (for example, ref. <sup>41</sup> and the references therein). For definitions and descriptions of the various ‘seepage’ terms used here, the reader may refer to refs. <sup>41,69–76</sup>. Details are provided in Supplementary Information 2.

For Martian geological context, we analysed image data from the MOLA on Mars Global Surveyor, as well as the Context Camera and High Resolution Imaging Science Experiment on Mars Reconnaissance Orbiter, incorporating information from published geological maps and reports. We initially evaluated a wide area (~1,000 km radius) surrounding Gale Crater. However, GCM simulations indicated that features more than ~800 km from Gale would be unlikely to account for the Gale detections. Emphasis was then placed on the grid areas used in the GCM simulations. All data were mapped using Esri’s ArcGIS software and the US Geological Survey Mars Global GIS version 2.1 (outline of the MFF from geological global map I-1802ABC). Details are provided in Supplementary Information 2.

### Data availability

The PFS data used in this study are publicly available via the ESA Planetary Science Archive. References of terrestrial gas seepage data are reported in the Supplementary Information. Data used to map water-equivalent hydrogen are available from J. T. Wilson (Johns Hopkins University Applied Physics Laboratory, [Jack.Wilson@jhuapl.edu](mailto:Jack.Wilson@jhuapl.edu)). All other geological data of Mars used in this study are in the public domain and include published papers, data provided in the US Geological Survey Mars Global GIS version 2.1 (which can be accessed on the Mars GIS FTP site: [ftp://pdsimage2.wr.usgs.gov/pub/pigpen/mars/Global\\_GIS\\_Mars/](ftp://pdsimage2.wr.usgs.gov/pub/pigpen/mars/Global_GIS_Mars/); file name: MarsGIS\_Equi0\_v21.zip (note that v21 is used in the file name for v2.1)), and Context Camera and Visible data image mosaics provided by Google Earth (Mars).

### Code availability

The core GEM model used for this work is publicly available through <http://collaboration.cmc.ec.gc.ca/science/rpn.comm/>. The routines that were modified for the application to Mars are explained in ref. <sup>39</sup> and available upon request from F.D. ([Frank.Daerden@aeronomie.be](mailto:Frank.Daerden@aeronomie.be)) and L.N. ([Lori.Neary@aeronomie.be](mailto:Lori.Neary@aeronomie.be)). The model output used in this paper is available upon request from F.D., L.N. and S.V. ([Sebastien.Viscardy@aeronomie.be](mailto:Sebastien.Viscardy@aeronomie.be)). The equations for the statistical analysis are included in the Methods. The computer code to reproduce the results is available from S.V.

### References

51. Levenberg, K. A method for the solution of certain non-linear problems in least squares. *Q. Appl. Math.* **2**, 164–168 (1944).
52. Marquardt, D. W. An algorithm for least-squares estimation of nonlinear parameters. *J. Soc. Ind. Appl. Math.* **11**, 431–441 (1963).
53. Ignatiev, N. I., Grassi, D. & Zasova, L. V. Planetary Fourier Spectrometer data analysis: fast radiative transfer models. *Planet. Space Sci.* **53**, 1035–1042 (2005).
54. Stamnes, K., Tsay, S. C., Wiscombe, W. & Jayaweera, K. Numerically stable algorithm for discrete-ordinate-method radiative transfer in multiple scattering and emitting layered media. *Appl. Opt.* **27**, 2502–2509 (1988).
55. Rothman, L. S. et al. The HITRAN2012 molecular spectroscopic database. *J. Quant. Spectrosc. Radiat. Transf.* **130**, 4–50 (2013).
56. Fiorenza, C. & Formisano, V. A solar spectrum for PFS data analysis. *Planet. Space Sci.* **53**, 1009–1016 (2004).
57. Kurucz, R. The solar spectrum: atlases and line identifications. In *Laboratory and Astronomical High Resolution Spectra* (eds Sauval, A. J., Blomme, R. & Grevesse, N.) Vol. 81, 17–31 (Astronomical Society of the Pacific, 1995).
58. Millour, E. et al. The Mars Climate Database (MCD version 5.2). In *European Planetary Science Congress 2015* 10 (Copernicus 2015).
59. Forget, F. et al. Improved general circulation models of the Martian atmosphere from the surface to above 80 km. *J. Geophys. Res.* **104**, 24155–24176 (1999).
60. Grassi, D. et al. Methods for the analysis of data from the Planetary Fourier Spectrometer on the Mars Express Mission. *Planet. Space Sci.* **53**, 1017–1034 (2005).
61. Wolkenberg, P. et al. Characterization of dust activity on Mars from MY27 to MY32 by PFS-MEX observations. *Icarus* **310**, 32–47 (2018).
62. Press, W. H., Teukolsky, S. A., Vetterling, W. T. & Flannery, B. T. *Numerical Recipes: The Art of Scientific Computing* 3rd edn (Cambridge Univ. Press, 2007).
63. Smith, M., Daerden, F., Neary, L. & Khayat, S. The climatology of carbon monoxide and water vapor on Mars as observed by CRISM and modeled by the GEM-Mars general circulation model. *Icarus* **301**, 117–131 (2018).
64. Musiolik, G. et al. Saltation under Martian gravity and its influence on the global dust distribution. *Icarus* **306**, 25–31 (2018).
65. Vandaele, A. C. et al. Science objectives and performances of NOMAD, a spectrometer suite for the ExoMars TGO mission. *Planet. Space Sci.* **119**, 233–249 (2015).
66. Robert, S. et al. Expected performances of the NOMAD/ExoMars instrument. *Planet. Space Sci.* **124**, 94–104 (2016).
67. Robert, S. et al. Two test-cases for synergistic detections in the Martian atmosphere: carbon monoxide and methane. *J. Quant. Spectrosc. Radiat. Transf.* **189**, 86–104 (2017).
68. Montabone, L. et al. Eight-year climatology of dust optical depth on Mars. *Icarus* **251**, 65–95 (2015).
69. Abrams, M. A. Significance of hydrocarbon seepage relative to petroleum generation and entrapment. *Mar. Petroleum Geol.* **22**, 457–477 (2005).
70. Etiopie, G. & Klusman, R. W. Microseepage in drylands: flux and implications in the global atmospheric source/sink budget of methane. *Global Planet. Change* **72**, 265–274 (2010).
71. Etiopie, G., Nakada, R., Tanaka, K. & Yoshida, N. Gas seepage from Tokamachi mud volcanoes, onshore Niigata Basin (Japan): origin, post-genetic alterations and CH<sub>4</sub>–CO<sub>2</sub> fluxes. *Appl. Geochem.* **26**, 348–359 (2011).
72. Klusman, R. W., Leopold, M. E. & LeRoy, M. P. Seasonal variation in methane fluxes from sedimentary basins to the atmosphere: results from chamber measurements and modeling of transport from deep sources. *J. Geophys. Res. Atmos.* **105**, 24661–24670 (2000).
73. Macgregor, D. S. Relationships between seepage, tectonics and subsurface petroleum reserves. *Mar. Petroleum Geol.* **10**, 606–619 (1993).
74. Malmqvist, L. & Kristiansson, K. A physical mechanism for the release of free gases in the lithosphere. *Geoexploration* **23**, 447–453 (1985).
75. Mazzini, A. & Etiopie, G. Mud volcanism: an updated review. *Earth Sci. Rev.* **168**, 81–112 (2017).
76. Schumacher, D. & Abrams M.A. (eds) *Hydrocarbon Migration and Its Near-Surface Expression*. AAPG Memoir 66, 446 (American Association of Petroleum Geologists, 1996).